JOM, Vol. 16, No. 1, 2015
DOI: 10.1007/s11837-014-1185-7
© 2014 The Minerals, Metals & Materials Society

High-Temperature Oxidation Behavior of Al-Co-Cr-Ni-(Fe or Si) Multicomponent High-Entropy Alloys

T.M.BUTLER,[1] J.P.ALFANO,[1] R.L.MARTENS,[2] and M.L.WEAVER[1,3]

1.—Department of Metallurgical and Materials Engineering, University of Alabama, Tuscaloosa, AL 35487, USA. 2.—Central Analytical Facility, University of Alabama, Tuscaloosa, AL 35487, USA. 3.—e-mail: mweaver@eng.ua.edu

High-entropy alloys (HEAs) are a class of alloys that are being considered for a number of applications. In the present study, the microstructures and 1050°C oxidation behaviors of two HEAs, $Al_{10}Cr_{22.5}Co_{22.5}Ni_{22.5}Fe_{22.5}$ (at.%) and $Al_{20}Cr_{25}Co_{25}Ni_{25}Si_5$ have been investigated along with $Al_{15}Cr_{10}Co_{35}Ni_{35}Si_5$, which is a high-temperature shape-memory alloy. Oxide formation occurred via selective oxidation in a manner that was consistent with the oxide formation model devised by Giggins and Pettit for model Ni-Cr-Al alloys. The lower Al content alloy formed an external Cr_2O_3 scale and an internal subscale consisting of Al_2O_3 and AlN precipitates. The higher Al content alloys exhibited smaller mass gains and formed external Al_2O_3 scales without any internal oxidation of the alloys.

INTRODUCTION

High-entropy alloys (HEAs) represent an emerging class of materials that is being investigated for a range of possible applications.[1–8] In contrast to conventional engineering alloys, HEAs lack a principal component and are generally composed of five or more primary metallic components in equiatomic or nearly equiatomic concentrations. Many HEAs tend to form simple face-centered cubic (fcc) and/or body-centered cubic (bcc)-type solid solution phases, a fact often attributed to their high entropies of mixing that are thought to suppress the formation of intermetallic compounds or other equilibrium phases. It has been proposed that the retention of simple solid-solution structures, either as monolithic entities or in conjunction with intermetallic precipitates, could lead to the development of new alloys exhibiting unique combinations of mechanical, physical, and chemical properties including: high ductility, hardness, and creep strength; good resistance to wear, corrosion, and oxidation; and high abnormally high microstructural stability.[1–16]

The majority of the studies performed on HEAs have addressed phase formation/selection criteria, phase stability, or understanding various mechanical, electrical, and chemical properties. In general, there have been very few investigations of the oxidation behaviors and mechanisms in multicomponent HEAs.[9,17–26] Most of these studied provided either no kinetic or microstructural information, and neglected the potential influences of HEA characteristics (i.e., the high-entropy effect). This article presents and compares the microstructural evolution of two Al-Co-Cr-Ni-(Fe or Si)-based HEAs and one ferromagnetic shape memory with a similar composition during oxidation at 1050°C in air. This study was conducted to provide some insights into the oxidation behavior of HEAs.

EXPERIMENTAL PROCEDURES

Bulk alloy buttons with the compositions of $Al_{10}Cr_{22.5}Co_{22.5}Ni_{22.5}Fe_{22.5}$ (designated AL10F), $Al_{20}Cr_{25}Co_{25}Ni_{25}Si_5$ (designated AL20S), and $Al_{15}Cr_{10}Co_{35}Ni_{35}Si_5$ (designated AL15S) were produced by arc melting raw materials with purities ≥99.5% on a water-cooled copper hearth under an inert argon atmosphere. Each button was remelted several times to promote uniformity. There were no significant differences between the nominal and analyzed alloy compositions (Table I).

Microstructural analysis was performed using a combination of x-ray diffraction (XRD), scanning electron microscopy (SEM), and transmission electron microscopy (TEM). Chemical analyses were done using energy dispersive x-ray spectroscopy (EDS) in both the SEM and TEM. TEM specimens

(Published online November 5, 2014)

Table I. Experimentally determined as-cast alloy and phase compositions (at.%)

Alloy	Region or phase	Crystal structure	Al	Co	Cr	Ni	Si	Fe
AL10F	Overall	–	10.19 ± 0.06	21.74 ± 0.08	22.64 ± 0.15	23.59 ± 0.18	–	21.84 ± 0.05
	Dendritic	fcc	9.45 ± 0.57	22.08 ± 0.49	22.81 ± 0.06	23.17 ± 0.60	–	22.49 ± 0.71
	Interdendritic	B2 + bcc	26.56 ± 1.20	15.52 ± 0.31	14.36 ± 1.21	30.93 ± 0.91	–	12.64 ± 0.60
	Matrix	B2	25.46 ± 0.51	16.58 ± 0.90	7.10 ± 1.85	39.46 ± 1.56	–	11.39 ± 1.10
	Ppt.	bcc	13.38 ± 0.09	17.69 ± 1.05	28.08 ± 0.24	27.20 ± 0.23	–	13.65 ± 1.12
AL20S	Overall	–	19.83 ± 0.50	24.33 ± 0.46	25.59 ± 0.20	24.30 ± 0.40	5.95 ± 0.26	–
	Dendritic	B2 + bcc	22.12 ± 0.10	24.58 ± 0.16	23.97 ± 0.13	25.06 ± 0.17	4.28 ± 0.06	–
	Matrix	B2	21.40 ± 0.14	25.04 ± 0.27	10.18 ± 0.15	39.31 ± 0.49	3.31 ± 0.06	–
	Ppt.	bcc	11.66 ± 0.09	31.12 ± 0.23	34.76 ± 0.21	25.40 ± 0.20	4.72 ± 0.06	–
	Interdendritic	B2 + σ	8.51 ± 0.07	26.37 ± 0.16	35.92 ± 0.15	20.27 ± 0.16	8.93 ± 0.07	–
	Low Z	B2	21.77 ± 0.22	25.04 ± 0.40	12.89 ± 0.25	36.97 ± 0.49	3.33 ± 0.09	–
	High Z	σ	1.93 ± 0.06	28.47 ± 0.39	53.05 ± 0.44	9.36 ± 0.23	7.18 ± 0.11	–
AL15S	Overall	–	15.17 ± 0.60	34.50 ± 0.35	10.37 ± 0.18	34.98 ± 0.50	4.98 ± 0.31	–
	Dendritic	fcc	6.89 ± 0.04	40.85 ± 0.14	13.37 ± 0.69	35.80 ± 0.13	3.08 ± 0.02	–
	Interdendritic	$L1_0$	21.30 ± 0.09	27.69 ± 0.18	5.50 ± 0.07	40.75 ± 0.21	4.75 ± 0.05	–

were made using a variation of the focused-ion beam (FIB) in situ lift-out method for TEM foil preparation in an FEI Quanta 200 3D Dual Beam FIB microscope (FEI Company, Hillsboro, OR).[27] XRD measurements were conducted on bulk specimens on a Philips X'pert MPD XRD (Philips, Amsterdam, The Netherlands) with Cu-Kα radiation operated at 45 kV and 40 mA. Cross-sectional images of the as-cast and oxidized microstructures were captured on a JEOL 7000F SEM (JEOL Ltd., Tokyo, Japan) in the backscattered mode. Bright-field TEM images, selected area diffraction patterns (SADPs), and high-angle annular dark-field (HAADF) images were captured on a 200-keV FEI Technai G^2 F-20 Supertwin scanning-transmission electron microscope (STEM). All TEM-EDS data were analyzed using FEI ES Vision software with thickness correction.[28]

Discontinuous isothermal oxidation tests were conducted in laboratory air at 1050°C on as-cast specimens for times ranging from 1 h to 1000 h. Prior to the start of testing, specimen surfaces were ground to a 1200-grit SiC surface finish on all sides and placed into individual Al_2O_3 boats. The specimens were systematically removed from the furnace at regular intervals to measure mass, image the oxidized surfaces, and to conduct XRD experiments. Many of those specimens were then returned to the furnace for further oxidation. Specimen mass was measured on an Orion Cahn C-34 microbalance (Thermo Electron Corporation, Beverly, MA) with a sensitivity of 1×10^{-6} g. Microstructural evolution during oxidation was investigated using the previously defined methods.

RESULTS AND DISCUSSION

Microstructures of the As-Cast Alloys

Macroscopically, the as-cast alloys consisted of coarse dendrites with varying degrees of segregation. In all cases, the dendrites appeared to exhibit orthogonal symmetries suggesting that the primary phases of solidification were cubic.[29–31] However, a closer examination via electron microscopy revealed the presence of complex transformation products in each alloy, the details of which are described below.

Figure 1 shows representative XRD patterns along with SEM and TEM images of the AL10F HEA in the as-cast state. This alloy consisted of medium atomic number contrast (i.e., medium Z-contrast) dendrites, labeled D, interspersed with lower Z-contrast interdendritic regions, labeled ID. The dendrites in this alloy, which had compositions that were close to the nominal composition of the alloy (Table I), were found to be single phase with an fcc crystal structure and a lattice parameter of $a_{fcc} = 3.599 \pm 0.005$ Å. In contrast, the interdendritic regions, which had higher concentrations of Ni and Al, consisted of two phases: a B2 matrix phase that was rich in Ni and Al ($a_{B2} = 2.875$ Å) and a high Z-contrast precipitate phase that was richer

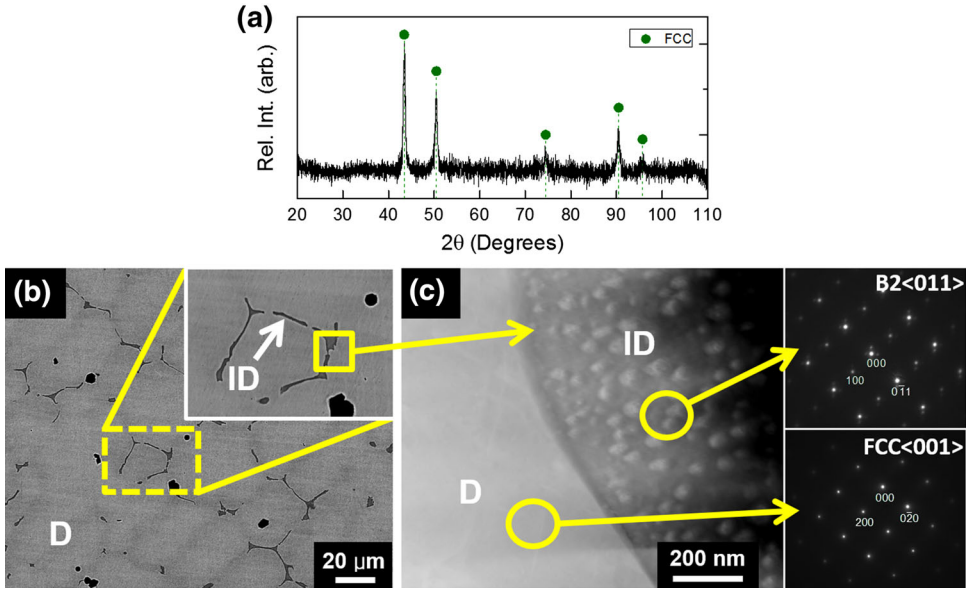

Fig. 1. Microstructure of the as-cast AL10F HEA: (a) XRD pattern, (b) SEM backscattered electron image showing medium Z-contrast dendrites (labeled D) separated by low *Z*-contrast interdendritic regions (labeled ID) with inset image collected at higher magnification, and (c) STEM-HAADF image showing high *Z*-contrast precipitates inside region ID regions and SADPs collected from regions D and ID.

in Cr and Co. Electron diffraction patterns were not obtained from the precipitates, but TEM-EDS showed them to be richer in Cr than the B2 matrix and the fcc dendrites. Recently, Wang et al.[32,33] reported similar microstructures in an Al-Co-Cr-Fe-Ni-based HEA that contained ~10 at.% Al and identified the precipitates as bcc. Further efforts are underway to identify the crystal structures of the precipitates; however, the inference that they are bcc is also consistent with the computational modeling efforts of Zhang et al.,[14] who predicted the formation of fcc, bcc, and B2 equilibrium phases in alloys in this composition range.

Figure 2 shows representative XRD patterns along with SEM, as well as the TEM images of the AL20S HEA in the as-cast state. This alloy consisted of low *Z*-contrast dendrites and higher *Z*-contrast interdendritic regions. The dendrites consisted of two phases: a darker matrix phase that was rich in Ni and Al as well as a brighter precipitate phase that was richer in Co and Cr. The precipitates ranged from nearly spherical to rectangular in shape. From the SADPs, the matrix and precipitates phases were found to have B2 and bcc crystal structures, respectively, with lattice parameters of $a_{B2} = 2.936 \pm 0.057$ Å and $a_{bcc} = 2.903 \pm 0.035$ Å. In agreement with the observations of Wang et al.,[32] the B2 and bcc phases were fully coherent exhibiting a cube-on-cube orientation relationship (i.e., $\langle 001\rangle_{B2}//\langle 001\rangle_{bcc}$). The interdendritic regions were composed of interconnected and alternating lamellae that were generally arranged into modulated net-like structures. From electron diffraction, the lamellae were found to consist of a Ni- and Al-rich B2 phase and a Co- and Cr-rich σ phase with lattice parameters of $a_{B2} = 2.902 \pm 0.049$ Å, $a_\sigma = 8.958 \pm 0.067$ Å, and $c_\sigma = 4.514 \pm 0.053$ Å, respectively. In some areas, these phases were arranged into packets that were reminiscent of the Widmanstätten structures often observed in Ti-based alloys and steels.[34] In many areas, the grain boundaries were also decorated with a semi-continuous high *Z*-contrast phase. Wang et al.[32,33] reported similar microstructures in Al-Co-Cr-Fe-Ni based HEAs containing ~15 to ~23 at.% Al.

Figure 3 shows representative XRD patterns along with SEM, and TEM images of the AL15S alloy in the as-cast state. This alloy contained two distinct microstructural features: (I) large, relatively featureless dendrites and (II) interdendritic regions that consisted of alternating light and dark bands. Similar microstructures have been reported in several Co-Ni-Al based ferromagnetic shape-memory alloys.[35–38] The dendrites, which were found to be rich in Ni, Co, and Cr (Table I), consisted of a disordered fcc matrix phase that was interspersed with nanometer-sized precipitates with $L1_2$ crystal structures. The fcc and $L1_2$ phases were found to be fully coherent and to exhibit a cube-on-cube orientation relationship (i.e., $\langle 001\rangle_{fcc}//\langle 001\rangle_{L12}$) and had lattice parameters of $a_{fcc} = 3.594$ Å and $aL12 = 3.583$ Å, respectively. Similar phase distributions were reported by Daoud et al.[39] in an $Al_8Co_{17}Cr_{17}Cu_8Fe_{17}Ni_{33}$ HEA. The interdendritic regions, which were richer in Ni and Al, consisted of a heavily twinned $L1_0$ phase with lattice parameters of $a_{L10} = 2.789$ Å and $c_{L10} = 2.968$ Å. Similar features have been reported in near-equiatomic Co-Ni-Al ferromagnetic shape-memory alloys and Ni-rich β-NiAl intermetallics, and they are known to evolve from a martensitic B2-to-$L1_0$ phase transformation.[35–38,40]

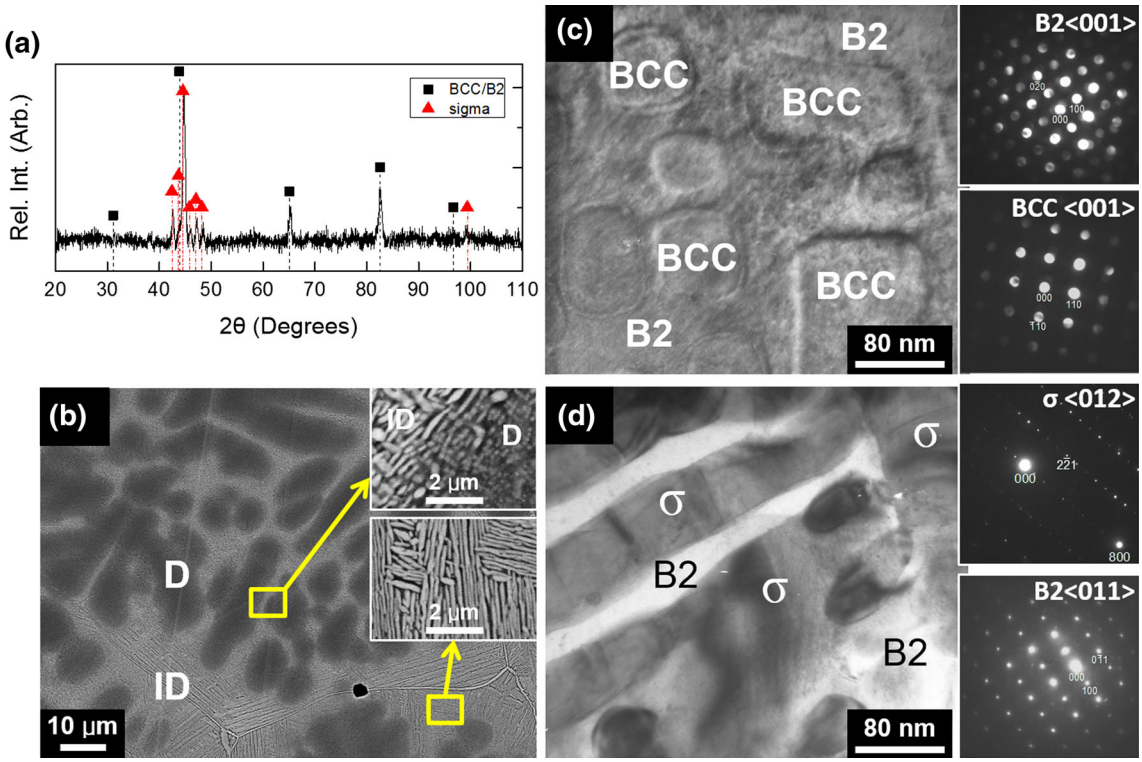

Fig. 2. Microstructure of the as-cast AL20S HEA: (a) XRD pattern, (b) SEM backscattered electron image showing the as-cast microstructure with inset images of the dendritic (D) and interdendritic (ID) regions, (c) bright-field (BF) TEM images and SADPs collected from region D, and (d) BF-TEM images and SADPs collected from region ID.

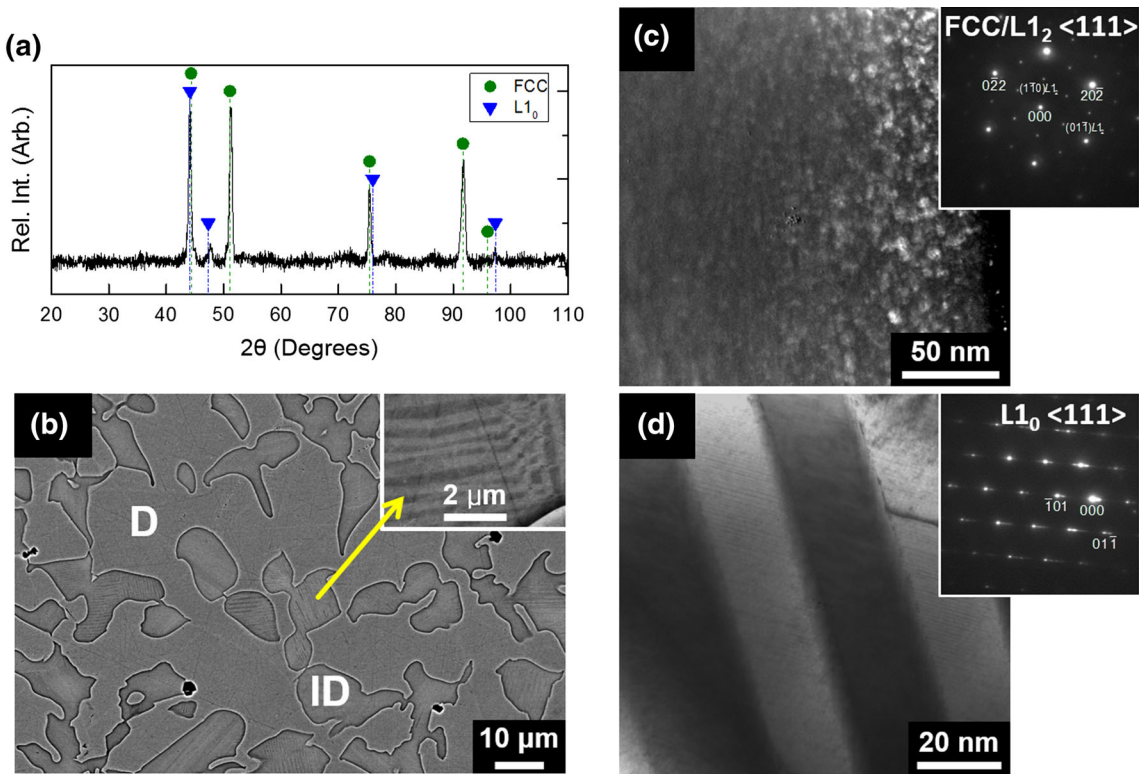

Fig. 3. Microstructure of the as-cast AL15 alloy: (a) XRD pattern, (b) SEM backscattered electron image showing the as-cast microstructure and an inset image of the transformed interdendritic region, (c) dark-field TEM image and SADP collected from region D, and (d) BF-TEM image and SADP collected from region ID.

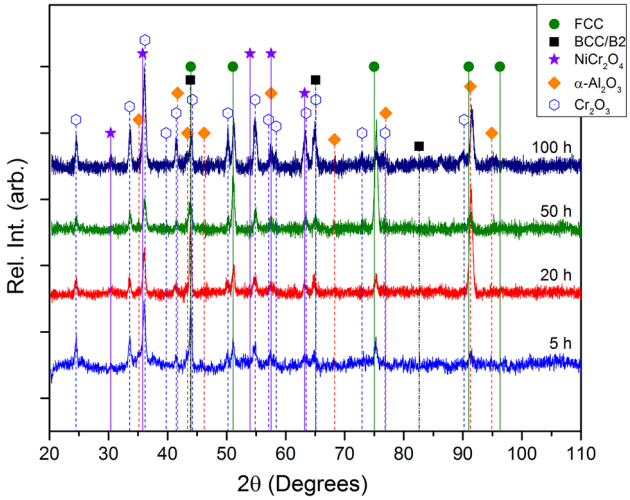

Fig. 4. XRD patterns from the AL10F HEA after oxidation at 1050°C for 5 h, 20 h, 50 h, and 100 h.

Oxidized Microstructures

Figures 4, 5, and 6 show representative XRD patterns, plus SEM and TEM images for the AL10F HEA after oxidation at 1050°C. For all oxidation times, fcc, α-Al_2O_3, and Cr_2O_3 XRD peaks were observed. The Al_2O_3 and Cr_2O_3 peaks intensified with increased oxidation time, indicating the growth of an external oxide scale. After 100 h of oxidation, an additional peak was observed near 30° 2θ which matched a $NiCr_2O_4$ spinel. No spinels were observed in the SEM or TEM specimens examined in this study; however, these types of phases are known to form on the outermost surfaces of ternary M-Cr-Al-type alloys (where M = Ni, Co, and/or Fe) during the early stages of oxidation.[41] After oxidation for 5 h (Fig. 5a–c), a discontinuous external Cr_2O_3 scale formed on the alloy surface along with an internal subscale consisting of coarse α-Al_2O_3 precipitates. Beneath the subscale, acicular AlN

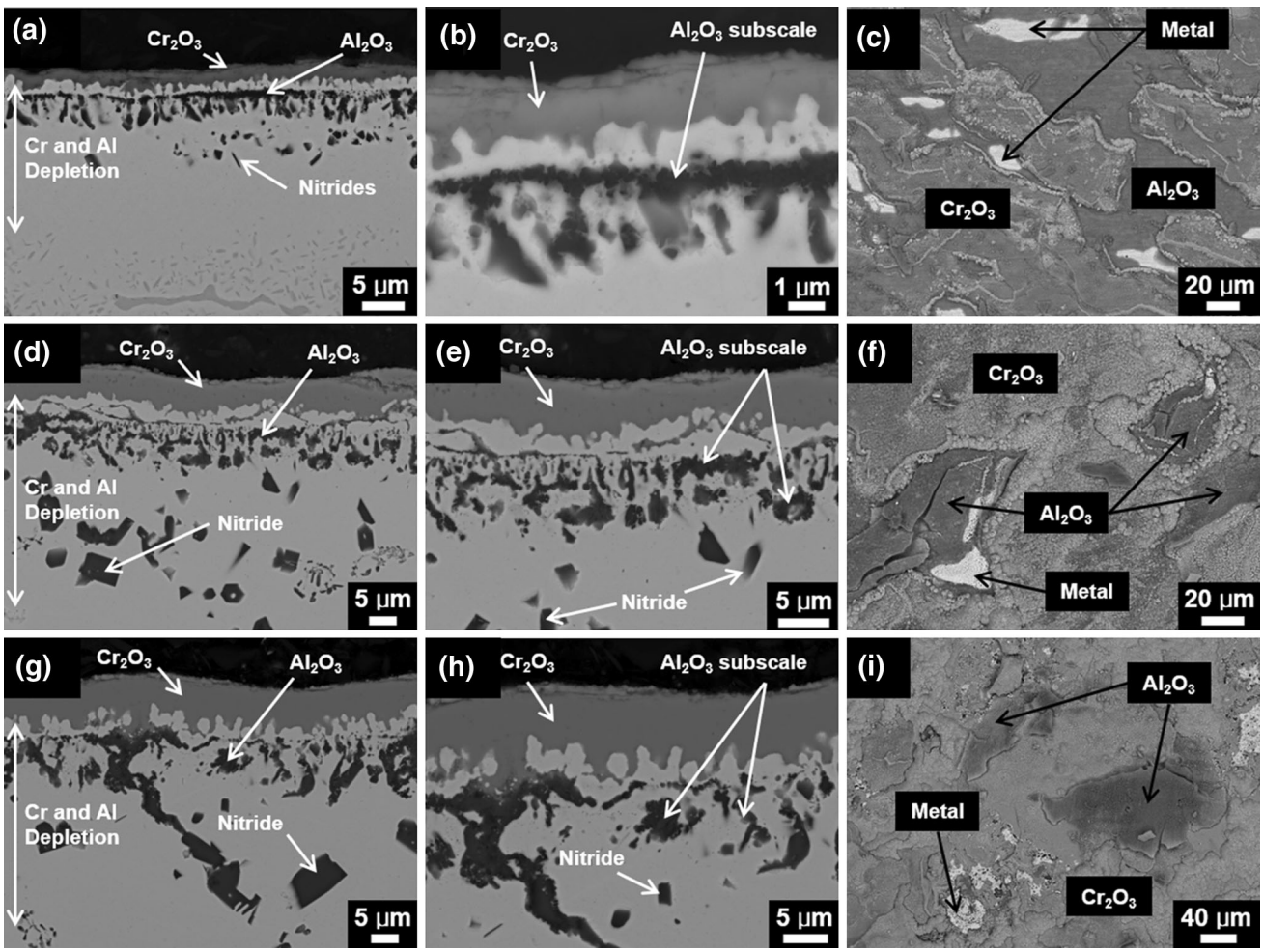

Fig. 5. SEM backscattered electron micrographs of the AL10F HEA after oxidation: (a–c) After 5 h of oxidation, (d–f) after 50 h of oxidation, and (g–i) after 100 h of oxidation.

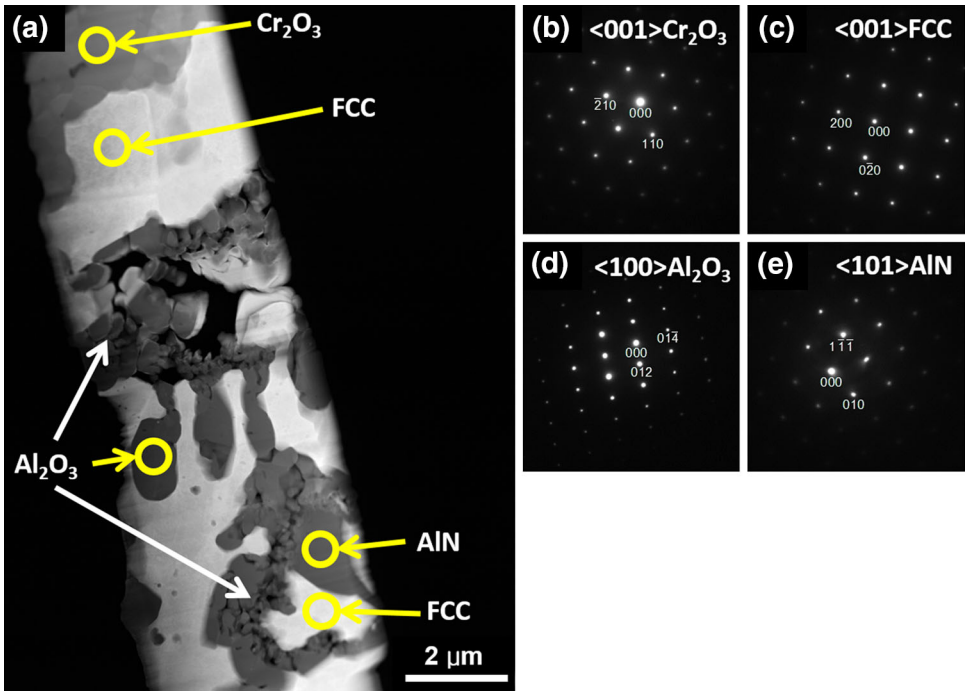

Fig. 6. Microstructure of an AL10F HEA that was oxidized at 1050°C for 50 h: (a) STEM-HAADF image of the specimen that was lifted out perpendicular to the oxide scales and corresponding SADPs confirming the presence of Cr_2O_3 (b), fcc (c), Al_2O_3 (d), and AlN (e) phases, respectively. The enclosed circles indicate the regions where the SADPs and the EDS data summarized in Table II were collected from.

precipitates were observed inside of an fcc phase that was severely depleted in Cr and Al. This fcc phase contained as much as 10 at.% oxygen in solid solution and was devoid of B2 or bcc precipitates. This can be seen more clearly in the STEM-HAADF image after 50 h of oxidation (Fig. 6) and in the EDS results presented in Table II, which clearly show the four phases.

Equivalent postoxidation microstructures have been reported in several model and commercial Ni-Cr-Al based alloys[41–47] and recently by Zhang et al.[19] in $Al_{0.5}FeCoCrNi$ and $Al_{0.5}CoCrFeNiSi_{0.2}$ HEAs oxidized at 900°C in air. Scale thickening and precipitate coarsening occurred as oxidation time increased (Fig. 5d–i).

Figures 7, 8, and 9 show representative XRD patterns plus SEM and TEM images for the AL20S HEA after oxidation for 20, 96, and 500 h, respectively. The XRD patterns contained bcc/B2, σ, α-Al_2O_3, and fcc peaks. The Al_2O_3 and fcc peak intensities increased with oxidation time, whereas the bcc/B2 and σ peak intensities remained relatively constant. In general, this alloy developed an external oxide scale that thickened with increasing oxidation time. The scales were composed of two oxide phases, α-Al_2O_3, which was the major phase, and Cr_2O_3, which was the minor phase. When observed, the Cr_2O_3 was almost always on top of the Al_2O_3 as can be seen in Fig. 8c, g, and h, but it was intermittent in appearance. Just beneath the scale, an Al-depleted zone formed consisting of a high Z-contrast fcc phase with a lattice parameter of a_{fcc} = 3.578 Å. This phase contained almost equal parts Cr and Co along with a high Ni concentration (Table II). In the interiors of the oxidized specimens, B2 and σ phases coarsened noticeably as oxidation time was increased.

Figure 10 shows representative XRD patterns for the AL15S alloy after oxidation for 20 h, 96 h, and 500 h. The patterns contained fcc, $L1_0$, and α-Al_2O_3 peaks. The intensities of the Al_2O_3 peaks appeared to increase slightly with increasing oxidation time. Figure 11 shows representative backscattered SEM images after oxidation at 1050°C. During oxidation, an external oxide scale formed coupled with coarsening of the underlying microstructure. The scale was primarily composed of α-Al_2O_3; however, in some areas small amounts of Cr_2O_3 were also observed either embedded in the Al_2O_3 or on top of it. The cracks observed beneath the oxide scale in Fig. 11a, c, d, and f are believed to have formed during metallographic sample preparation. Internally, the microstructure was composed of fcc, $L1_2$, and $L1_0$ phases (Figs. 12 and 13). Like the as-cast alloy, the $L1_2$ phase formed as nanoscale precipitates within the fcc phase (Fig. 12b and c) along with twinned plates in the $L1_0$ regions (Fig. 12d and e). Just beneath the oxide scale, a continuous layer of the fcc/$L1_2$ phase mixture formed, presumably due to Al depletion (Fig. 13). This layer had nearly the same composition as the fcc/$L1_2$ regions

Table II. Chemical compositions of the phases observed in the alloys after various periods of oxidation at 1050°C (at.%)

Alloy	Phase or region	Al	Co	Cr	Ni	Si	Fe	O	N
AL10F	Scale/external	–	–	38.92 ± 0.40	–	–	–	60.82 ± 1.75	–
50 h	FCC/subscale	0.04 ± 0.07	23.85 ± 0.53	13.47 ± 0.27	25.76 ± 1.11	–	26.92 ± 1.14	9.94 ± 3.00	–
	Al_2O_3/subscale	39.15 ± 3.16	0.01 ± 0.03	0.40 ± 0.44	0.02 ± 0.03	–	0.01 ± 0.02	60.38 ± 3.14	–
	AlN	46.82 ± 2.62	–	–	–	–	–	–	53.18 ± 2.61
	FCC/interior	0.15 ± 0.05	23.03 ± 1.43	13.77 ± 1.32	24.43 ± 1.15	–	24.43 ± 1.43	–	–
AL20S	Scale/external	0.05 ± 0.07	0.08 ± 0.11	38.92 ± 0.40	0.05 ± 0.06	–	0.05 ± 0.07	60.84 ± 0.06	–
96 h	FCC/subscale	2.94 ± 0.11	35.21 ± 0.27	29.85 ± 0.92	21.65 ± 0.25	3.46 ± 0.22	–	6.87 ± 1.34	–
	B2/interior	19.41 ± 0.95	24.85 ± 0.40	10.84 ± 0.45	39.32 ± 0.51	2.64 ± 0.26	–	2.91 ± 0.38	–
	σ/interior	0.92 ± 0.11	27.23 ± 0.21	49.06 ± 0.17	10.33 ± 0.33	5.35 ± 0.16	–	7.10 ± 0.52	–
AL15S	Scale/external	38.62 ± 1.72	–	0.39 ± 0.07	–	0.15 ± 0.04	–	60.82 ± 1.75	–
96 h	FCC/subscale	4.86 ± 0.58	40.16 ± 0.61	13.51 ± 0.27	33.32 ± 1.25	3.65 ± 0.62	–	4.46 ± 0.54	–
	FCC/interior	5.79 ± 0.70	41.49 ± 0.04	14.35 ± 0.47	32.95 ± 0.23	5.41 ± 0.50	–	–	–
	$L1_0$/interior	22.83 ± 1.63	25.52 ± 1.00	4.24 ± 0.33	43.13 ± 1.43	4.26 ± 0.44	–	–	–

The data points for AL10F, AL20S, and AL15S are noted on Figs. 8, 12, and 13, respectively

observed in the center of the alloy; however, it contained ~4 at.% oxygen in solid solution (Table II). No oxygen was detected in the centers of the oxidized specimens. Microstructural coarsening continued through 500 h of oxidation, ultimately leading to some scale spallation and the formation of voids beneath the fcc layer.[48] These voids typically form due to the Kirkendall effect.[49–53]

Oxidation Behavior

Figure 14 shows normalized mass change data for each alloy after oxidation testing at 1050°C. Included on this figure for comparison is some recent oxidation data for $Al_8Cr_{23}Co_{23}Ni_{23}Fe_{23}$ and $Al_{12}Cr_{22}Co_{22}Ni_{22}Fe_{22}$ HEAs (labeled AL8F and AL12F, respectively).[54] All three alloys gained mass with increasing oxidation time at levels that were comparable to those reported by Giggins and Pettit for model Ni-Cr-Al alloys,[41] and for some commercial and experimental structural alloys[42–47] oxidized between 1000°C and 1200°C. The AL15S alloy exhibited the smallest total mass gains followed by the AL20S and AL10F HEAs, respectively.

An analysis of the mass gains indicated that oxidation occurred via subsequent transient and parabolic stages. In the AL10F and AL20S HEAs, the transient oxidation stages appeared to end when the specimens were removed from the furnace the first time for weighing. This was particularly evident in the second AL10F specimen, which was oxidized in 24-h increments. Upon reinsertion into the furnace for further oxidation, those alloys transitioned to parabolic growth. In the AL20S HEA no further mass gain was detected for experiments running longer than ~40 h. The AL15S alloy also exhibited an initial transient stage of oxidation. This region, however, was followed by a region of significant mass loss during which significant scale spallation occurred. Upon reloading, approximately parabolic growth ensued. No further mass changes were observed for experiments running longer than 140 h.

There was no evidence of breakaway oxidation in any of the specimens. Parabolic rate constants determined from the slopes of $(\Delta W/A)^2$ versus t plots are summarized for each alloy in Table III.

The calculated values for each alloy were consistent with our experimental observations in that the AL10F HEA formed an external Cr_2O_3 scale, whereas the AL20S HEA and AL15S alloy formed external α-Al_2O_3 scales.

Naturally, the formation of external Al_2O_3 and Cr_2O_3 scales produces Al and/or Cr depleted regions beneath the scales. Table IV summarizes the oxide scale and depleted zone thicknesses after various oxidation times.

Some representative phase compositions were presented in Table II. The compositions tabulated in that table were collected from the regions denoted

on Figs. 6, 9, 12, and 13. From the data, it is evident that significant amounts of subsurface Cr and Al depletion occurred in the AL10F HEA, which resulted in the formation of the observed subsurface fcc phase. This phase, which contained almost no Al, had more than 10 at.% oxygen in solid solution. As oxidation time increased, the oxide scale and depleted zone thicknesses increased in a manner that was similar to that of other Cr_2O_3-forming alloys.[55,56] Based on the amounts of Cr and Al depletion, it can be inferred that this alloy would eventually lose its capacity to form a protective scale at 1050°C. The AL20S HEA and AL15S alloy also exhibited significant Al depletion, which resulted in the formation of the observed subsurface fcc phase. In the AL20S HEA, the oxide scale and Al-depleted zone increased in thickness as oxidation time was increased. In the AL15S alloy, the oxide scales and Al-depleted zones showed virtually no change in thickness from 20 h to 500 h. In the AL20S HEA and AL15S alloy, the subsurface fcc phases contained large enough quantities of Al to promote the formation of an external Al_2O_3 scale. For example, the fcc phase in the AL15S alloy contained approximately 5 at.% Al, which is well above the level needed to impart favorable oxidation resistance in Ni-Cr-Al alloys.[41,57]

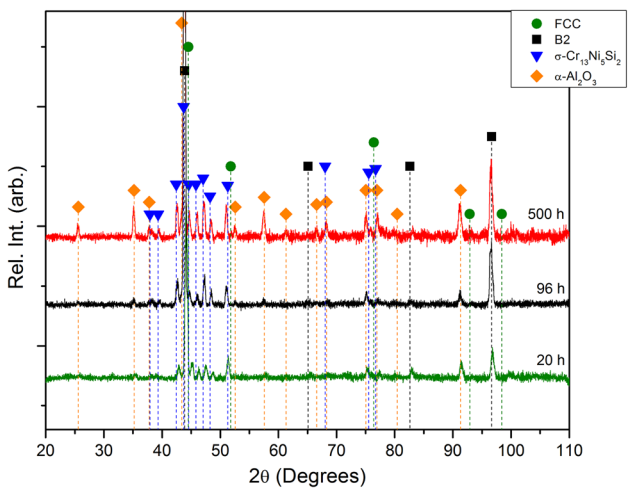

Fig. 7. XRD patterns from the AL20S HEA after oxidation at 1050°C for 20 h, 96 h, and 500 h.

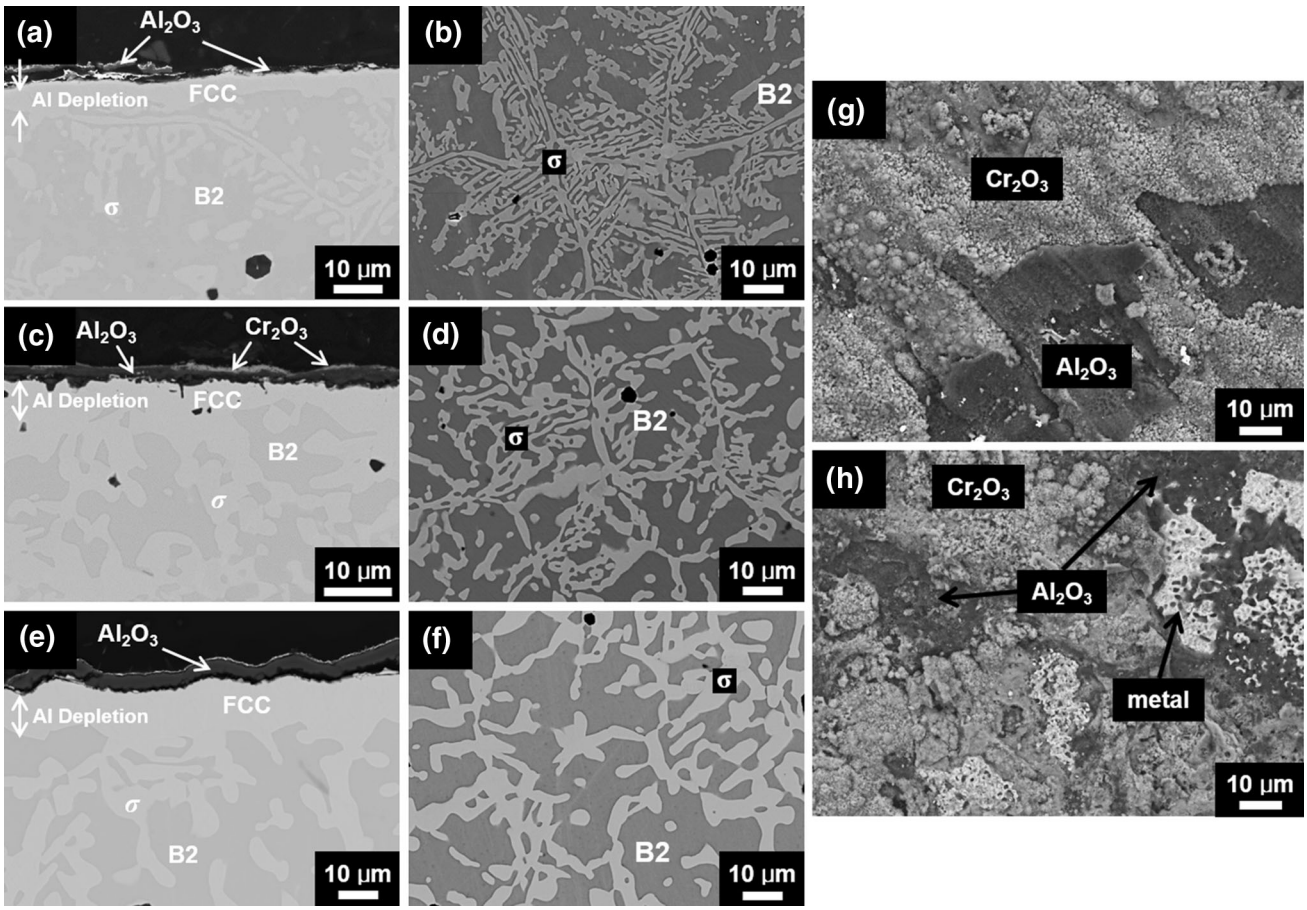

Fig. 8. Backscattered electron micrographs of the oxide scale and underlying microstructure of the AL20S HEA after (a and b) 20 h, (c and d) 96 h, and (e and f) 500 h of oxidation at 1050°C. Plan view backscattered electron micrographs of the oxide scale (g) 10 h and (h) 100 h of oxidation.

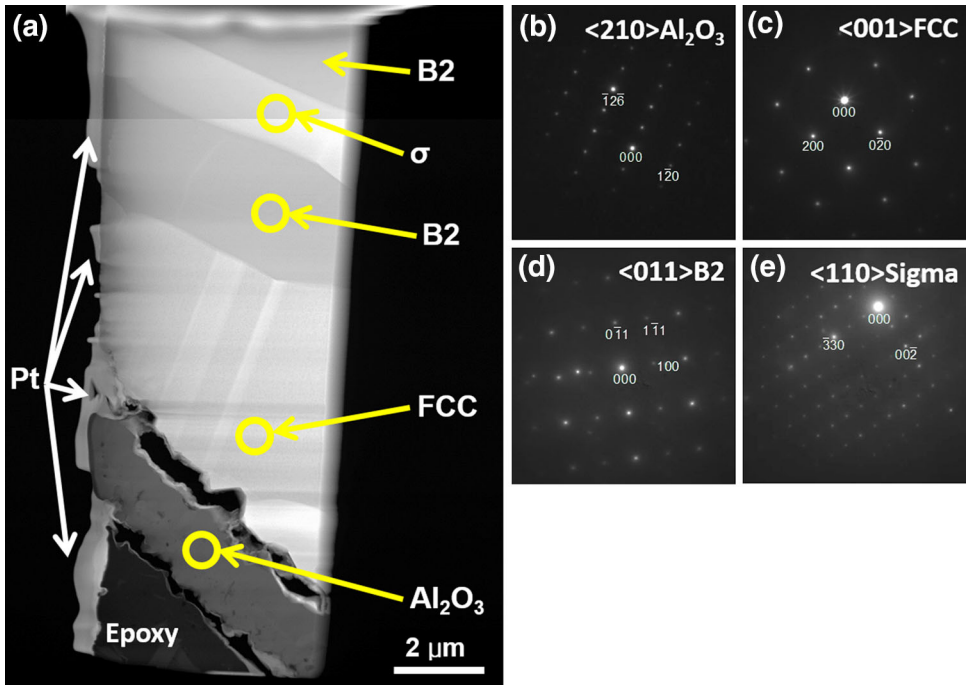

Fig. 9. Microstructure of the AL20S HEA after oxidation at 1050°C for 96 h. (a) Mosaic STEM-HAADF image of a specimen that was lifted out perpendicular to the oxide scales and corresponding SADPs confirming the presence of (b) Al_2O_3, (c) fcc, (d) B2, and (e) sigma phases, respectively. The enclosed circles indicate the regions where the SADPs and the EDS data summarized in Table II were collected from.

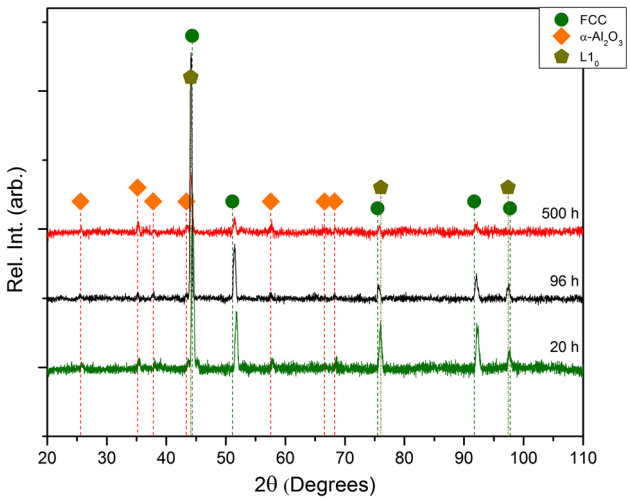

Fig. 10. XRD patterns from the AL15 alloy after oxidation at 1050°C for 20 h, 96 h, and 500 h.

Comparison with Conventional Oxidation-Resistant Alloys

Alloys intended for use in high-temperature oxidizing environments rely on the formation of an external oxide scale that provides resistance to oxidation and hot corrosion. To be protective, this scale must be chemically, mechanically, and thermodynamically stable. Conventional oxidation-resistant alloys have been designed to form slow-growing, continuous, and adherent surface scales consisting of Al_2O_3, Cr_2O_3, or SiO_2. For example, the heat-resistant stainless steels that are widely used for energy production and chemical processing have been designed to form Cr_2O_3 scales. In contrast, many commercial Ni-based superalloys have been designed to form Al_2O_3 scales. The Al_2O_3 scales grow at slower rates, are thermodynamically more stable, and provide protection to higher temperatures than Cr_2O_3 scales, which are compromised in aggressive environments (e.g., water vapor, carbon, sulfur, etc.).[51–53] It has been surmised that HEAs could exhibit better resistances to corrosion, oxidation, and interdiffusion than conventional structural alloys or intermetallics.[2,24,58–60] This is due in large part to their reported tendencies toward reduced diffusivities,[61,62] improved damage tolerances,[6] and higher concentrations of oxide-forming elements (in solid solution or precipitates).

Some insights into the oxidation behaviors of Al-Co-Cr-Ni-(Fe or Si)-based HEAs can be obtained by considering the well-documented oxidation behaviors of model Ni-Cr-Al, Co-Cr-Al, and Fe-Cr-Al alloys.[41] In all three systems, oxidation occurs via succeeding transient and steady-state stages. Transient oxidation begins with the conversion of a thin layer of the alloy surface into oxides and concludes with the development of these oxides into a continuous external scale. During this stage, oxide growth generally proceeds via a linear rate law. The oxides that form during this transient stage are determined by alloy composition. For example, in model Ni-Cr-Al alloys, the transient oxides are

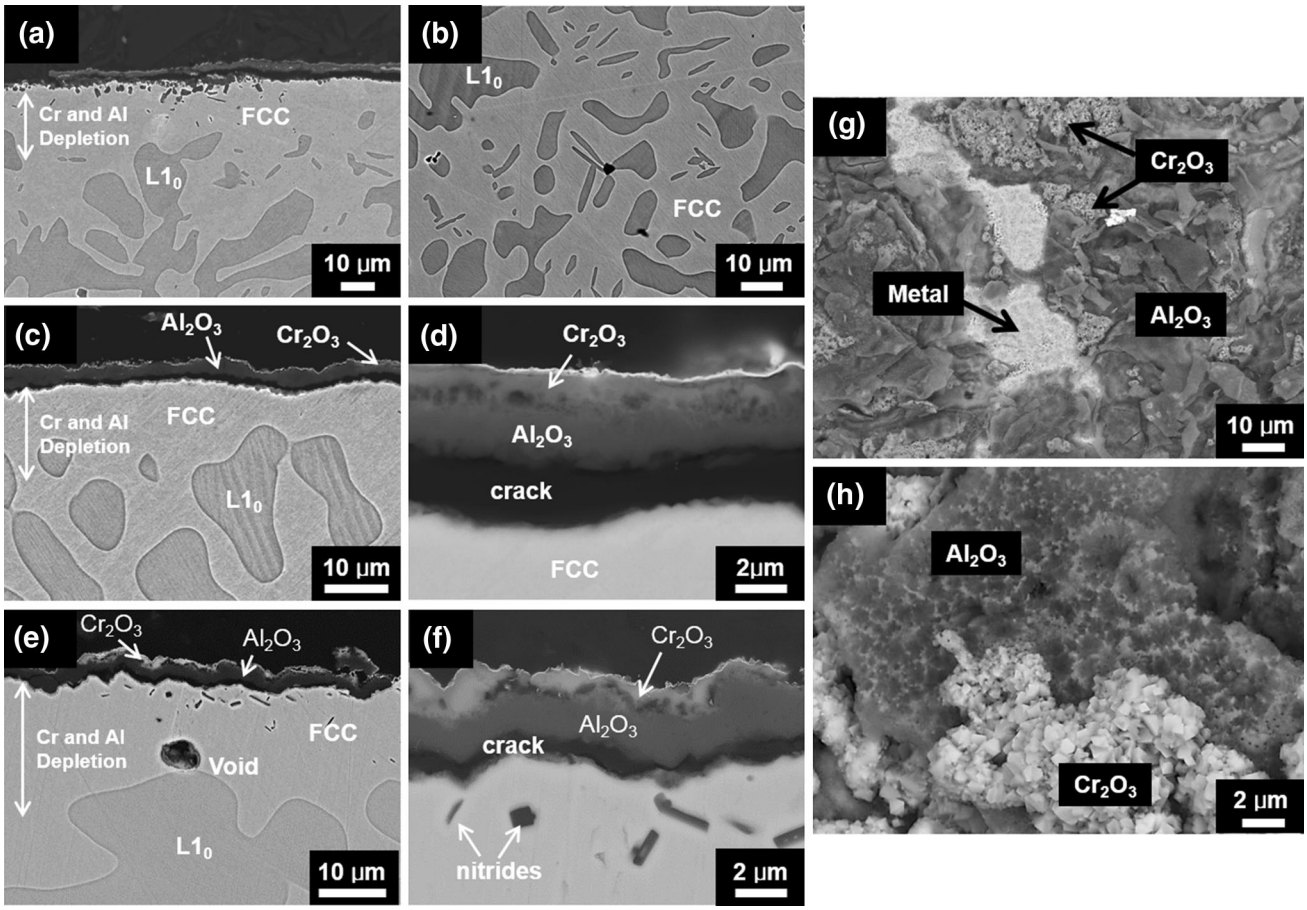

Fig. 11. Backscattered electron micrographs of the oxide scale and underlying microstructure of the AL15 alloy after (a and b) 20 h, (c and d) 96 h, and (e and f) 500 h of oxidation at 1050°C. Plan view backscattered electron micrographs of the oxide scale (g) 10 h and (h) 100 h of oxidation. The cracking observed in (c) and (f) were a result of sample preparation.

predominantly NiO and/or $Ni(Cr,Al)_2O_4$, although significant amounts of Al_2O_3 and Cr_2O_3 can also be present. Because transient oxidation occurs with very little diffusion, it is usually completed within 1 h but has been observed to last more than 20 h in some alloys.[41] Once the transient oxide becomes continuous, diffusion within the alloy leads to the formation of a subscale beneath the transient layer consisting of a mixture of Al_2O_3 and Cr_2O_3. This is accompanied by a transition from linear to parabolic kinetics. Ultimately, the evolution of the transient layer and the subscale, both of which depend upon alloy composition, determine the operative oxidation mechanism.

Figure 15 shows a schematic oxide map for the ternary Ni-Cr-Al system at 1000°C and 1100°C.[41,57] It is important to note that oxide maps are qualitative in nature, only representing the summary of empirical, experimental data/observations for a given alloy system. Superimposed on this map are data points for the three alloys investigated in this study. To facilitate presentation, the Ni, Fe, and Co contents (at.%) for the investigated alloys have been combined into a single term (i.e., Ni + Fe + Co). Similarly, the Si content has been incorporated into the Cr term (i.e., Cr + Si). The Ni-Cr-Al oxide map can be subdivided into three regimes:

1. Group I corresponds to dilute alloys where the Cr and Al concentrations are too low to establish continuous Cr_2O_3 or Al_2O_3 scales. Instead, the external scales consist of NiO plus $NiCr_2O_4$ and $Ni_2Al_2O_4$ spinel phases coupled with significant internal oxidation of Al. In this regime, the oxidation rates are determined by the diffusion of Ni in the NiO phase constituting the external scale.
2. Group II corresponds to alloys with large enough Cr concentrations, but relatively low Al concentrations, such that selective oxidation of Cr is promoted resulting in an external Cr_2O_3 scale. In these alloys, internal oxidation of Al occurs resulting in an internal subscale of Al_2O_3. In this regime, the oxidation process is largely determined by the diffusional growth of the external Cr_2O_3 scale.
3. Group III corresponds to alloys containing large enough Al concentrations to promote the selective oxidation of Al resulting in an external Al_2O_3 scale. In this regime, the oxidation process is

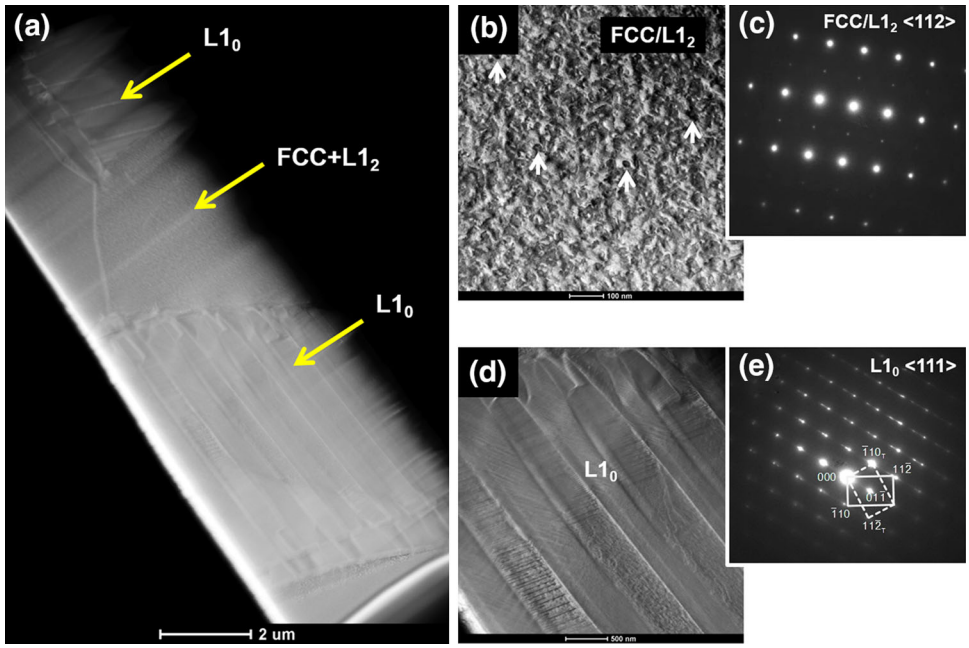

Fig. 12. Microstructure of the AL15 MEA that was oxidized at 1050°C for 96 h. (a) STEM-HAADF image collected from the center of the oxidized alloy, (b) higher magnification image of the fcc region indicating the presence of nanoscale $L1_2$ precipitates, (c) SADP from the fcc/$L1_2$ region, (d) higher magnification image of the $L1_0$ region indicating the presence of twinned martensite plates, and (e) SADP from the $L1_0$ phase. The enclosed circles indicate the regions where the SADPs and the EDS data summarized in Table II were collected from.

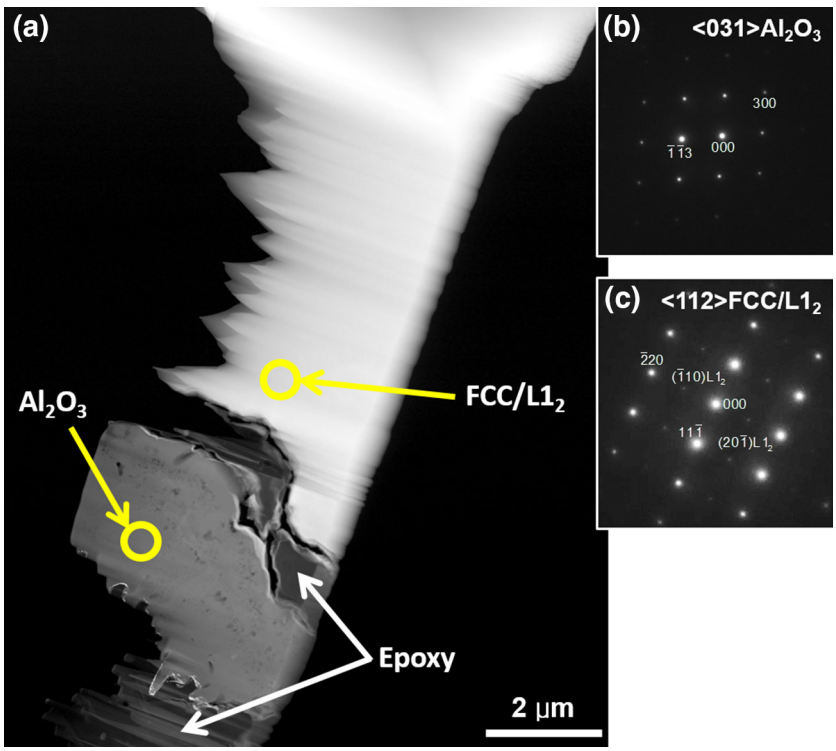

Fig. 13. Microstructure of the AL15 MEA that was oxidized at 1050°C for 96 h. (a) STEM-HAADF image of a specimen that was lifted out perpendicular to the oxide scales and corresponding SADPs confirming the presence of (b) Al_2O_3 and (c) fcc phases, respectively. The enclosed circles indicate the regions where the SADPs and the EDS data summarized in Table II were collected from.

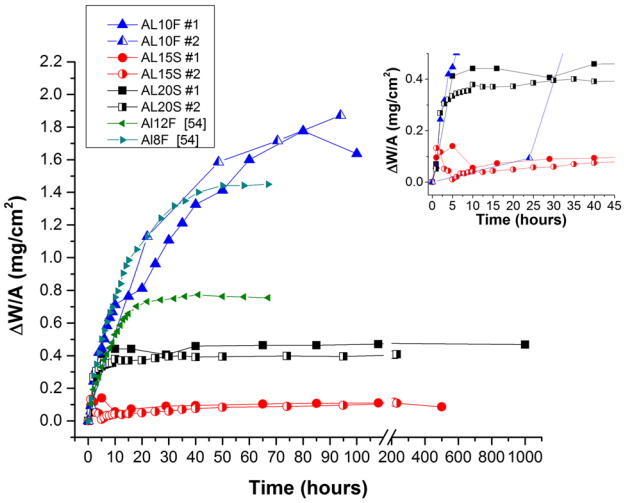

Fig. 14. Mass change results for all three alloys after discontinuous isothermal oxidation testing at 1050°C. The inset plot illustrates the early stages of oxidation for the AL10F, AL15S, and AL20S alloys.

Table III. Parabolic rate constants for the investigated alloys

Alloy	Sample #	k_P (g^2/cm^4 s)	Primary oxides formed
AL10F	1	$\sim 1.1 \times 10^{-11}$	Cr_2O_3 w/Al_2O_3 subscale
	2	$\sim 1.5 \times 10^{-11}$	
AL20S	1	5.1×10^{-15}	Al_2O_3 w/minor Cr_2O_3
	2	5.8×10^{-15}	
AL15S	1	3.6×10^{-15}	Al_2O_3 w/minor Cr_2O_3
	2	2.3×10^{-14}	

Table 4. Variation of oxide scale and depleted zone thickness with oxidation time

Alloy	Time (h)	Scale thickness (μm)	Depleted zone thickness (μm)
AL10F	1	–	5.3 ± 0.9
	5	1.82 ± 0.3	19.3 ± 1.7
	20	2.4 ± 0.5	26.9 ± 1.4
	50	6.7 ± 1.7	59.4 ± 4.5
	100	7.7 ± 1.3	73.3 ± 10.1
AL20S	20	1.5 ± 0.4	5.3 ± 1.0
	96	2.1 ± 0.7	7.3 ± 2.8
	500	3.3 ± 0.5	11.5 ± 1.1
AL15S	20	3.0 ± 1.2	18.3 ± 4.4
	96	2.7 ± 0.7	15.1 ± 3.7
	500	2.9 ± 0.2	18.0 ± 8.3

determined by the diffusional growth of the external Al_2O_3 scale.

Similar maps have been constructed for the ternary Co-Cr-Al[63] and Fe-Cr-Al[64] systems, with each showing similar types of oxidation products but different composition ranges. In each system, the

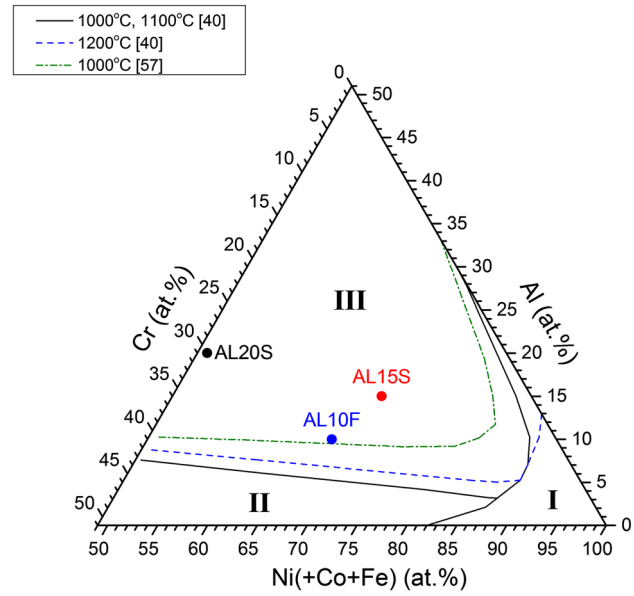

Fig. 15. Schematic oxide map for the ternary Ni-Cr-Al system at 1100°C.[41,57] On this figure, InOx means internal oxide.

oxidation mechanisms and products ultimately depend on the solubility and diffusion of oxygen plus the concentration and diffusion of the Al and/or Cr within the alloy.

The present experimental results (i.e., the post-oxidation microstructures and oxidation kinetics) were found to compare favorably with those of model Ni-Cr-Al alloys.[41,65] For example, the AL10F HEA lies near the apparent transition between Groups II and III on the Ni-Cr-Al oxide map, which suggests that a mixture of Cr_2O_3, Al_2O_3, and internal oxides should form. Experimentally this alloy, which was less oxidation resistant, formed an external Cr_2O_3 scale, a discontinuous internal Al_2O_3 subscale, and internal AlN precipitates during oxidation at 1050°C. This behavior is synonymous with Group II Ni-Cr-Al alloys oxidized in air.[41–43] In contrast, the AL20S HEA and the AL15S alloy, both of which lie within Group III on the Ni-Cr-Al oxide map and were more oxidation resistant, formed the expected external Al_2O_3 scales.[41] In general, these results suggest that the high-temperature oxidation behaviors of Al-Co-Cr-Ni-(Fe or Si) containing HEAs, like model Ni-Cr-Al alloys, are largely dictated by the relative concentrations of Al and Cr. However, no consistent behavioral trend could be identified to generally define the oxidation behaviors of HEAs aside from the qualitative observation that alloys with higher Al contents have smaller mass gains and tend to form Al_2O_3 scales. Smialek and Meier[66] have made similar observations for Ni-based superalloys, specifically noting that their complex chemistries in comparison to model M-Cr-Al alloys often overrode or obscured the general effects of Al and Cr.

The long-term oxidation behaviors of these alloys depend on the subsurface Al and/or Cr contents and

the depth of elemental depletion caused by scale formation. Increased depletion can reduce the ability of an alloy to reform a protective scale. As a result, a depleted surface may form less protective oxides when exposed to oxygen. Alloys with higher Al concentrations tended to form thinner, more protective oxide scales.

Much work remains to elucidate the oxidation behavior of HEAs. Earlier in this document it was noted that HEAs offered the potential for providing better oxidation resistance. Senkov et al.[24] demonstrated such a benefit in a refractory HEA system that they attributed to a combination of reduced diffusion rates for alloying elements, the formation of multiple complex oxides, and a reduction in the diffusivity and solubility of oxygen. However, the experimental results for the two Al-Co-Cr-Ni-(Fe or Si) HEAs examined in this study are inconclusive. The present study has demonstrated that selective oxidation occurs resulting in the formation of an external scale in a manner that is consistent with model M-Cr-Al alloys, commercial Ni-based superalloys, and stainless steels. However, what could not be determined is whether the diffusion kinetics were any slower or they exerted any influence on oxide growth. Experiments designed to carefully measure diffusivities and partitioning coefficients in oxidizing and nonoxidizing environments would be beneficial in this regard. Experimentation on well-annealed alloys would also be beneficial. Microstructural and chemical variations present in cast HEAs (even solid-solution HEAs) are certain to lead to nonuniform oxidation characteristics as have been reported in model alloy systems.[41] Further work is also necessary to optimize chemistries to form the desired oxides whilst still maintaining the favorable characteristics of HEAs in the underlying metal. Some useful guidance can be obtained from previous development efforts on alumina-forming austenitic (AFA) stainless steels,[67,68] spinodal Fe-Ni-Al based alloys,[69] and Alnico permanent magnet alloys,[70] which are all compositionally and morphologically quite similar to the presently studied HEAs.

SUMMARY AND CONCLUSION

The as-cast microstructures and oxidation behaviors of two Al-Co-Cr-Ni-(Fe or Si) multicomponent HEAs were investigated along with one Al-Co-Cr-Ni-Si based alloy.

1. Oxidation of the AL10F HEA at 1050°C led to the formation of a discontinuous, external Cr_2O_3 scale along with an internal Al_2O_3 subscale and AlN precipitates. In this alloy, the Al contents were too low to form a continuous Al_2O_3 subscale. As a result, this alloy gained mass through the duration of testing. Mass gain measurements reveal that the AL10F HEA tends to follow a parabolic growth law after an initial transient period. This behavior is analogous to many austenitic stainless steels and Cr_2O_3-forming superalloys.
2. Oxidation testing of the AL20S HEA and AL15S alloy at 1050°C resulted in the formation of continuous external Al_2O_3 scales with a small volume fraction of Cr_2O_3. As expected, the Al_2O_3 scale thickness increased with longer oxidation times. Both of these alloys tended to obey a parabolic growth law after an initial period of transient oxidation. No internal oxidation was detected in either of the alloys. The microstructures of the AL20S and AL15S alloys remained relatively stable with extended periods of high-temperature exposure.
3. The experimental results showed that all three alloys oxidized in accordance with the models proposed by Giggins and Pettit to explain the oxidation behaviors of Ni-Cr-Al alloys.

ACKNOWLEDGEMENT

This work used resources owned and maintained by the Central Analytical Facility (CAF), which is supported by the University of Alabama.

REFERENCES

1. W.-H. Wu, C.-C. Yang, and J.-W. Yeh, *Ann. Chim. Sci. Mater.* 31, 737 (2006).
2. J.W. Yeh, Y.L. Chen, S.J. Lin, and S.K. Chen, *Mater. Sci. Forum* 560, 1 (2007).
3. J.W. Yeh, S.K. Chen, S.J. Lin, J.Y. Gan, T.S. Chin, T.T. Shun, C.H. Tsau, and S.Y. Chang, *Adv. Eng. Mater.* 6, 299 (2004).
4. B. Cantor, I.T.H. Chang, P. Knight, and A.J.B. Vincent, *Mater. Sci. Eng. A* 375–377, 213 (2004).
5. Y. Zhang and Z. Yunjun, *Mater. Sci. Forum* 561–565, 1337 (2007).
6. D.B. Miracle, J.D. Miller, O.N. Senkov, C. Woodward, M.D. Uchic, and J. Tiley, *Entropy* 16, 494 (2014).
7. J.-W. Yeh, *JOM* 65, 1759 (2013).
8. Y. Zhang, T.T. Zuo, Z. Tang, M.C. Gao, K.A. Dahmen, P.K. Liaw, and Z.P. Lu, *Progr. Mater. Sci.* 61, 1 (2014).
9. P.K. Huang, J.W. Yeh, T.T. Shun, and S.K. Chen, *Adv. Eng. Mater.* 6, 74 (2004).
10. T.-T. Shun, C.-H. Hung, and C.-F. Lee, *J. Alloys Compd.* 493, 105 (2010).
11. J.M. Zhu, H.M. Fu, H.F. Zhang, A.M. Wang, H. Li, and Z.Q. Hu, *Mater. Sci. Eng. A* 527, 7210 (2010).
12. A. Cunliffe, J. Plummer, I. Figueroa, and I. Todd, *Intermetallics* 23, 204 (2012).
13. S. Guo, Q. Hu, C. Ng, and C.T. Liu, *Intermetallics* 41, 96 (2013).
14. C. Zhang, F. Zhang, S. Chen, and W. Cao, *JOM* 64, 839 (2012).
15. A.K. Singh and A. Subramaniam, *J. Alloy Compd.* 587, 113 (2014).
16. F. Zhang, C. Zhang, S.L. Chen, J. Zhu, W.S. Cao, and U.R. Kattner, *CALPHAD* 45, 1 (2014).
17. S.-T. Chen, W.-Y. Tang, Y.-F. Kuo, S.-Y. Chen, C.-H. Tsau, T.-T. Shun, and J.-W. Yeh, *Mater. Sci. Eng. A* 527, 5818 (2010).
18. J. Jiang and X. Luo, *Adv. Mater. Res.* 652–654, 1115 (2013).
19. H. Zhang, Q.T. Wang, Q.H. Tang, and P.Q. Dai, *Corros. Protec.* 34, 561 (2013).
20. M.-H. Chuang, M.-H. Tsai, W.-R. Wang, S.-J. Lin, and J.-W. Yeh, *Acta Mater.* 59, 6308 (2011).
21. M.-H. Hsieh, M.-H. Tsai, W.-J. Shen, and J.-W. Yeh, *Surf. Coat. Technol.* 221, 118 (2013).

22. C. Huang, Y. Zhang, J. Shen, and R. Vilar, *Surf. Coat. Technol.* 206, 1389 (2011).
23. C.M. Liu, H.M. Wang, S.Q. Zhang, H.B. Tang, and A.L. Zhang, *J. Alloy Compd.* 583, 162 (2014).
24. O.N. Senkov, S.V. Senkova, D.M. Dimiduk, C. Woodward, and D.B. Miracle, *J. Mater. Sci.* 47, 6522 (2012).
25. W.J. Shen, M.H. Tsai, K.Y. Tsai, C.C. Juan, C.W. Tsai, J.W. Yeh, and Y.S. Chang, *J. Electrochem. Soc.* 160, C531 (2013).
26. K.-H. Cheng, C.-W. Tsai, S.-J. Lin, and J.-W. Yeh, *J. Phys. D Appl. Phys.* 44, 205405 (2011).
27. D. Tomus and H.P. Ng, *Micron* 44, 115 (2013).
28. ES Vision (FEI-Company, Hillsboro, OR, 2004).
29. M.C. Flemmings, *Solidification Processing* (New York: McGraw-Hill, 1974).
30. W. Kurz and D.J. Fisher, *Fundamentals of Solidification* (Dürnten: Trans Tech Publications Ltd., 1998).
31. H. Fredriksson and U. Åkerlind, *Materials Processing During Casting* (Hoboken: Wiley, 2006).
32. W.-R. Wang, W.-L. Wang, S.-C. Wang, Y.-C. Tsai, C.-H. Lai, and J.-W. Yeh, *Intermetallics* 26, 44 (2012).
33. W.-R. Wang, W.-L. Wang, and J.-W. Yeh, *J. Alloy Compd.* 589, 143 (2014).
34. R.E. Reed-Hill and R. Abbaschian, *Physical Metallurgy Principles, Second Edition* (Boston: PWSKent, 1992).
35. B. Bartova, N. Wiese, D. Schryvers, J.N. Chapman, and S. Ignacova, *Acta Mater.* 56, 4470 (2008).
36. H.E. Karaca, I. Karaman, D.C. Lagoudas, H.J. Maier, and Y.I. Chumlyakov, *Scripta Mater.* 49, 831 (2003).
37. P.L. Potapov, P. Ochin, J. Pons, and D. Schryvers, *Acta Mater.* 48, 3833 (2000).
38. Y. Tanaka, T. Ohmori, K. Oikawa, R. Kainuma, and K. Ishida, *Metall. Mater. Trans.* 45, 427 (2004).
39. H.M. Daoud, A. Manzoni, R. Volkl, N. Wanderka, and U. Glatzel, *JOM* 65, 1805 (2013).
40. D. Schryvers, P. Boullay, P.L. Potapov, R.V. Kohn, and J.M. Ball, *Int. J. Solids Struct.* 39, 3543 (2002).
41. C.S. Giggins and F.S. Pettit, *J. Electrochem. Soc.* 118, 1782 (1971).
42. U. Krupp and H.J. Christ, *Metall. Mater. Trans. A* 31, 47 (2000).
43. S. Han and D.J. Young, *Oxid. Met.* 55, 223 (2001).
44. H. Ackermann, G. Teneva-Kosseva, H. Köhne, K. Lucka, S. Richter, and J. Mayer, *Mater. Corros.* 59, 380 (2008).
45. M.P. Brady, Y. Yamamoto, B.A. Pint, M.L. Santella, P.J. Maziasz, and L.R. Walker, *High Temperature Corrosion and Protection of Materials*, ed. P. Steinmetz, I.G. Wright, A. Galerie, D. Monceau, and S. Mathieu (Dürnten: TransTech Publications Ltd., 2008), pp. 725–732.
46. I. Peter, A. Zago, M. ActisGrande, and D. Ugues, *Surf. Coat. Technol.* 203, 1776 (2009).
47. C. Jang, D. Kim, D. Kim, I. Sah, W.-S. Ryu, and Y.-S. Yoo, *Trans. Nonfer. Metals Soc. China* 21, 1524 (2011).
48. J.P. Alfano (Ph.D. dissertation, The University of Alabama, 2013).
49. G.B. Gibbs and R. Hales, *Corros. Sci.* 17, 487 (1977).
50. Y. Shida, G.C. Wood, F.H. Stott, D.P. Whittle, and B.D. Bastow, *Corros. Sci.* 21, 581 (1981).
51. P. Kofstad, *High Temperature Corrosion* (New York: Elsevier, 1988).
52. N. Birks, G.H. Meier, and F.S. Pettit, *High-Temperature Oxidation of Metals*, 2nd ed. (Cambridge: Cambridge University Press, 2006).
53. D. Young, *High Temperature Oxidation and Corrosion of Metals* (Philadelphia: Elsevier, 2008).
54. T.M. Butler and M.L. Weaver, The University of Alabama, unpublished research (2014).
55. V.P. Deodeshmukh, S.J. Matthews, and D.L. Klarstrom, *Int. J. Hydrog. Energy* 36, 4580 (2011).
56. X. Ledoux, S. Mathieu, M. Vilasi, Y. Wouters, P. Del-Gallo, and M. Wagner, *Oxid. Met.* 80, 25 (2013).
57. G.R. Wallwork and A.Z. Hed, *Oxid. Met.* 3, 171 (1971).
58. J.-W. Yeh, *Ann. Chim. Sci. Mater.* 31, 633 (2006).
59. S.-Y. Chang, C.-E. Li, Y.-C. Huang, H.-F. Hsu, J.-W. Yeh, and S.-J. Lin, *Structural and Thermodynamic Factors of Suppressed Interdiffusion Kinetics in Multi-component High Entropy Materials (Scientific Report)* (New York: Macmillan Publishers Limited, 2014).
60. Z. Tang, L. Huang, W. He, and P.K. Liaw, *Entropy* 16, 895 (2014).
61. K.Y. Tsai, M.H. Tsai, and J.W. Yeh, *Acta Mater.* 61, 4887 (2013).
62. S.C. Middleburgh, D.M. King, G.R. Lumpkin, M. Cortie, and L. Edwards, *J. Alloy Compd.* 599, 179 (2014).
63. G.R. Wallwork, *Oxid. Met.* 3, 213 (1971).
64. P. Tomaszewicz and G.R. Wallwork, *Rev. High Temp. Mater.* 4, 75 (1978).
65. F.H. Stott and G.C. Wood, *Corros. Sci.* 11, 799 (1971).
66. J.L. Smialek and G.H. Meier, *Superalloys II*, ed. C.T. Sims, N.S. Stoloff, and W.C. Hagel (New York: Wiley, 1987), pp. 293–326.
67. Y. Yamamoto, M.P. Brady, Z.P. Lu, P.J. Maziasz, C.T. Liu, B.A. Pint, K.L. More, H.M. Meyer, and E.A. Payzant, *Science* 316, 433 (2007).
68. M.P. Brady, Y. Yamamoto, Z.P. Lu, P.J. Maziasz, C.T. Liu, B.A. Pint, and M.L. Santella, *Stainl. Steel World* 20, 1 (2008).
69. I. Baker, H. Wu, X. Wu, M.K. Miller, and P.R. Munroe, *Mater. Charact.* 62, 952 (2011).
70. R.D. Heidenreich and E.A. Nesbitt, *J. Appl. Phys.* 23, 352 (1952).